


Land use/cover change and the urbanization process in the Wuhan area from 1991 to 2013 based on MESMA

Anchang Sun¹ · Tao Chen¹  · Rui-qing Niu¹ · John Charles Trinder²

Received: 2 June 2015 / Accepted: 22 August 2016 / Published online: 29 August 2016
© Springer-Verlag Berlin Heidelberg 2016

Abstract Rapid urbanization leads to rapid land use/cover change that can cause a severe deterioration of living environment in urban areas. Although numerous research projects have explored land use/cover change and the urbanization process with remote sensing data, only a few have focused on the analysis of their temporal and spatial variations in a visualized method using sub-pixel imaging techniques. In this study, Wuhan, the largest developing city in Central China, was chosen as the experimental region. Six scenes from Landsat images were selected, covering a lengthy period. To solve the problem of mixed pixels in urban areas, the spectrum of each image was selected individually and multiple endmember spectral mixture analysis (MESMA), a sub-pixel imaging soft classification technique, was applied. The land-use dynamic and time-series land-cover fractional maps were produced to evaluate the land use/cover change situation. Next, the land-cover change intensity was calculated and the dominant land-cover change intensity is proposed as a virtualized method of analyzing the urbanization process during each period covered by the Landsat images. The results of the study demonstrate that the land-cover categories and fractional information were effectively acquired following the implementation of MESMA. This information shows that the built-up areas in Wuhan have expanded at an average rate of 4.36 % rate in the last 20 years. The

urbanization process has resulted in the transformation of the natural landscape to anthropogenic urban built-up areas. It is surprised that these transformations have not been smooth. In addition, the urbanization process exhibits different patterns during each period.

Keywords Remote sensing · Sub-pixel classification · Multiple endmember spectral mixture analysis · Land use/cover change · Urbanization

Introduction

In the past 20 years, land use/cover change has become the core domain and focus of frontier projects investigating global change (Chen 1997). The process of urbanization transforms the natural landscape to anthropogenic urban land use, leading to changes in the physical characteristics of the surface of the transformed areas (Huang et al. 2015). For instance, urban areas are developed through the alteration of other land-cover types, including forests, vegetated areas, lake areas and agricultural fields. In particular, the urbanization rate in China is the highest among Asian countries (Montgomery 2008). According to the United Nations (2012), it is projected that China's urban population will reach more than one billion by 2050. This massive population and rapid urban growth are likely to cause both significant changes in land use and land cover and severe environmental deterioration (Weng and Quattrochi 2007). These changes will also cause a loss of agricultural land, increasing the risk of soil and water pollution and regional climate change (Chen et al. 2011a, b). As a result, there is an increasing need to map and monitor urban land use/cover change and urbanization process.

✉ Tao Chen
taochen@cug.edu.cn

¹ Institute of Geophysics and Geomatics, China University of Geosciences, Wuhan 430074, China

² Surveying and Geospatial Engineering, School of Civil and Environmental Engineering, The University of New South Wales, Sydney, NSW 2052, Australia

In recent years, satellite remote sensing techniques have been widely used because of their comprehensive and regular coverage (Zhao et al. 2003). Because of the complexity of urban surfaces, medium- or coarse-resolution sensors cannot detect urban features such as urban buildings and infrastructure directly within the sensor's field of view (Alan et al. 1986). In these situations, the sensors actually measure reflections from the terrain surface with proportional weighting according to the contributions of the features covered by each pixel instead of recording the intensity of a single feature; thus, they generate mixed pixels. Mixed pixels have long been recognized as a problem that influences the effective use of remotely sensed data in urban land use/cover change classifications (Cracknell 1998; Fisher 1997; Niu et al. 2014). Traditional classification methods, such as maximum likelihood classifiers, will inappropriately categorize the pixel as a single land type, thus affecting the accuracy of the classification. Spectral mixture analysis (SMA) has been developed to solve this problem. A spectral mixture model is a physically based model in which a mixed spectrum is modeled as a combination of pure spectra, called endmembers (Adams et al. 1993). Linear SMA derives the fractional contribution of endmember materials by modeling image spectra as a linear combination of endmembers, leading to more accurate and reliable classifications. SMA is widely used to solve the mixed-pixel problem in land-cover classifications, especially in urban areas. Small et al. (2001, 2002) use linear SMA to study the variations of urban vegetation in time and space, whereas Lu and Weng (2006) use SMA to extract a city's impervious surface with an accuracy of 83.78 %.

However, SMA has limitations. It does not account for spectral variations present within the same material given that it permits only one endmember per material (Dennison and Robert 2003). In other words, the pixels can only be modeled by stationary spectral combination. Roberts et al. (1998) propose multiple endmember spectral mixture analysis (MESMA) based on SMA. This method dynamically adjusts the number of endmembers in processing each mixed pixel. Theoretically, MESMA can handle an unlimited number of endmember spectra. It evaluates and selects the best endmember spectra from all possible combinations for each pixel (Rosso et al. 2005). MESMA has been applied to map urban land cover at the sub-pixel level and describe urban material distributions (Powell et al. 2007; Powell and Roberts 2010; Rashed et al. 2003; Michishita et al. 2012b). These studies show that MESMA can be applied to remotely sensed data with robust results for remotely sensed data.

Although previous research has explored land use/cover change and urban extent using MESMA, only a few studies have analyzed their temporal and spatial variation using

long time-series remote sensing data in a visualized method. Moreover, it is very difficult to build a public spectral library for long-time-range data because the atmosphere situations are different for each acquisition of images. This study uses MESMA to acquire land-cover categories and fractional information over the 20 years of the research period. Wuhan, the largest developing city in Central China, was chosen as the experimental region. The spectra of each image were selected individually to avoid the influence of atmospheric effects. After MESMA, modeling information and fraction information were combined to analyze land use/cover change situations. Next, time-series land-cover fractional maps were drawn to explore the urbanization process in relation to land-cover change in a visualized manner. Finally, land-cover change intensity (LCCI) is calculated and the dominant LCCI (DLCCI) was extracted to summarize the pattern of Wuhan's urbanization process.

Description of the study area

Wuhan, the capital of Hubei Province, is located in the east of Jiangnan Plain at the intersection point of the Yangtze River and the Han River (113°41'E~115°05'E, 29°50'N~31°22'N). It is composed of three towns—Wuchang, HanKou and Hanyang—and covers an area of 8494.41 km². It has a subtropical monsoon climate with four seasons, adequate illumination and abundant rainfall. Wuhan is a flat, watery land that is crisscrossed by rivers and lakes. It is the most flourishing city in central China and has a population of 8.217 million. According to the Wuhan Municipal Bureau of Statistics (2012), Wuhan's gross domestic product reached 905.127 billion yuan in 2013, nearly 40 times that in 1991. The city's rapid economic growth and huge population imply an urban explosion over the last 20 years.

The city of Wuhan now has seven main districts and six rural districts. This study focuses on the seven main districts because it includes the majority of the urban areas (Fig. 1).

Materials and methods

Data and preprocessing

Five Landsat-5 Thematic Mapper (TM) images and one Landsat-8 Operational Land Imager (OLI) image, provided by International Scientific & Technical Data Mirror Site (<http://www.gscloud.cn>), were used in this study (Table 1). These image products were carefully selected using appropriate time intervals to limit seasonal variations.

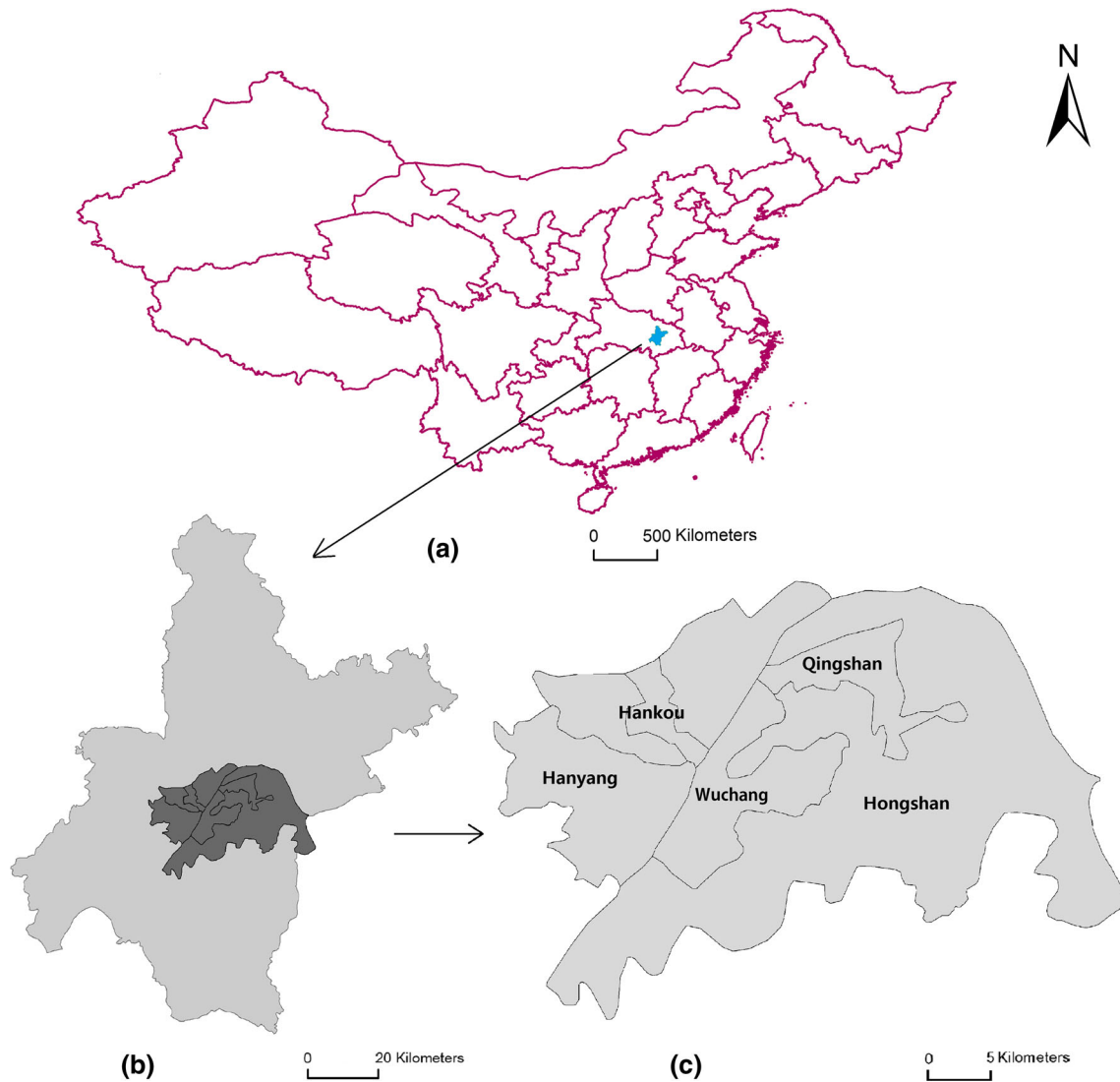


Fig. 1 Location of the study area **a** the location of Wuhan area in China; **b, c** the study area in Wuhan

Table 1 Landsat images used in this study

Satellite	Orbit	Time
Landsat 5	P123r039	1991.10.23
		1996.10.04
		2000.10.31
		2005.09.11
Landsat 8	P123r039	2009.09.06
		2013.10.03

The data preprocessing procedure is shown in Fig. 2 (top of the rectangle). These images are all level 1T products that have already been corrected for radiation and geometry. The 1991 image was used as the reference for the registration to ensure that all images have

consistent geometric characteristics. The nearest-neighbor resample method was used in this step, and the root mean square error (RMSE) in the transformations of the remaining scenes to the reference was limited to within 0.5 pixels. Then, a vector file was generated through vectorization to resize the six time-series images. All of these steps were performed using the ENVI 5.0 software platform. The entire flow chart for this study is shown in Fig. 2.

Multiple endmember spectral mixture analysis

Linear spectral mixture model

The SMA decomposes mixed pixels as a combination of estimates of the pure spectra of land components, which

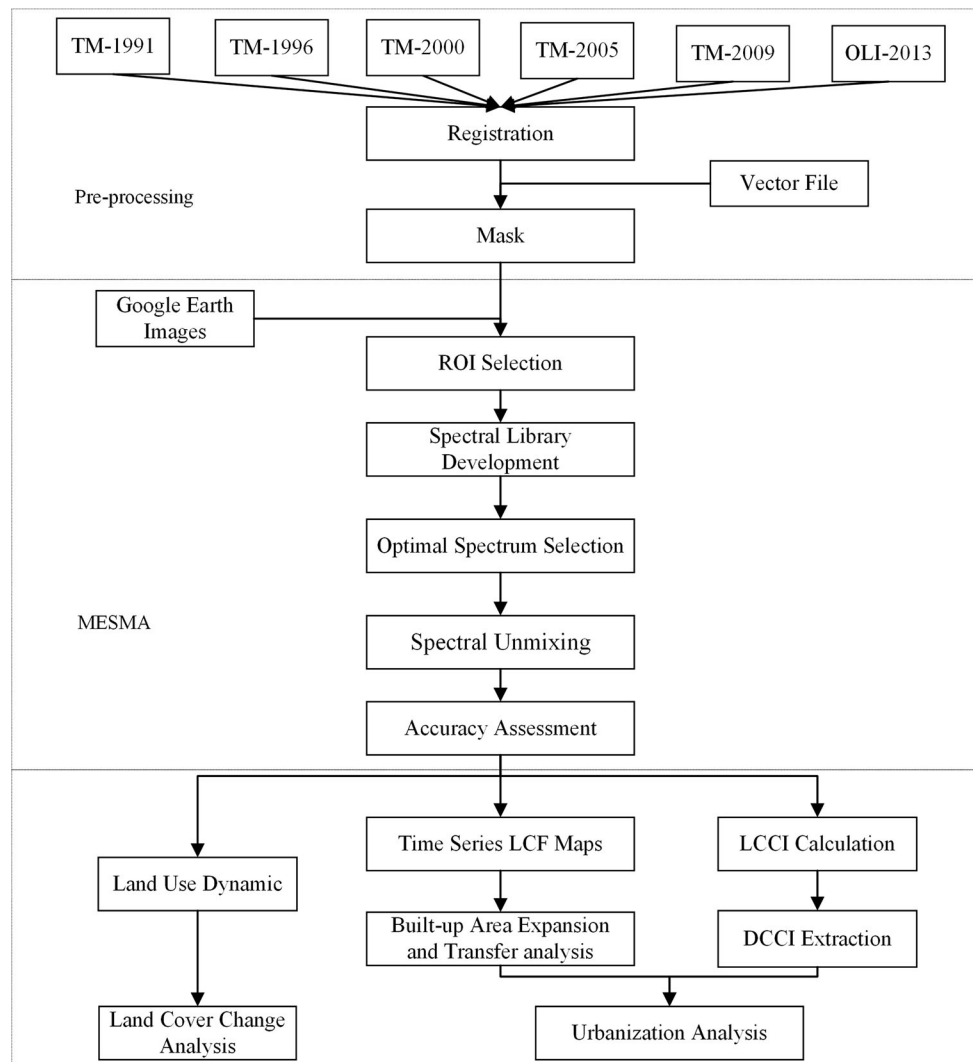


Fig. 2 Flow chart for this study

are the endmembers (Zhao et al. 2003). A common linear spectral model defines the pixel reflectance as a combination of endmembers’ reflectance and their proportion in the pixel area. It can be expressed as follows:

$$R_{i\lambda} = \sum_1^N f_i X \rho_{i\lambda} + \varepsilon_\lambda \tag{1}$$

$$\sum_1^N f_i = 1 \tag{2}$$

Here, $R_{i\lambda}$ is the reflectance of pixel i in band λ and N is the number of endmembers. $\rho_{i\lambda}$ indicates the reflectance of each endmembers, and ε_λ is the residual error. f_i is the fraction of each endmember that is commonly constrained by Eq. (2). The result is assessed using the root mean square error (RMSE):

$$RMSE = \sqrt{\frac{\sum_{\lambda=1}^M \varepsilon_\lambda^2}{M}} \tag{3}$$

where M is the band of the sensor. High RMSE indicates a poor estimate of endmembers.

The linear model separates and extracts the fractional spectral endmembers in the mixed pixels and determines its residual error in the image. The linear SMA has a definite physical meaning, which should lead to higher accuracy and is widely used in various applications for different landscapes. However, it fails to account for the existence of materials that are not included in endmembers. It also does not account for spectral variations in the same material because it permits only one endmember per material.

MESMA addresses these concerns by allowing endmembers to vary on a per-pixel basis (Roberts et al.

1998, 1999). Thus, the optimal endmembers are determined by three criteria: fraction, RMSE and the residuals for contiguous bands. An appropriate threshold of these three criteria should be set to produce the optimal candidate. The steps are shown at the middle of Fig. 2 (middle of the rectangle) and are explained in the following section.

Endmember extraction

Endmember extraction, which is a key step in SMA and MESMA, can be derived from an image or from field reflectance spectra. In practice, image-based endmember selection methods are frequently used because they readily obtain and represent the spectra measured on the same scale as the image data. Thus, the endmembers are extracted from the six time-series images used in this study.

The extracted endmembers must represent the ground material accurately and comprehensively (Dennison and Robert 2003). There are two challenges related to building a spectral library of mixed pixels. First, the spectral library should be sufficiently large to represent the variation in ground material. Second, with an increasing number of endmembers, the efficiency of calculation decreases (Michishita et al. 2012a). Therefore, we refer to the concept proposed by Ridd, who assumes that the spectral signature of land cover in urban environments is a linear combination of three components: vegetation, impervious surface and soil (Ridd 1995). Considering the land-cover characteristics of Wuhan, after several trials, four categories of endmembers are defined: (1) water; (2) green vegetation; (3) built-up area; and (4) bare land. The definitions of these categories in Wuhan are as follows:

1. Water (W) means all types of water area, such as rivers, lakes, paddy fields and fisheries.
2. Green vegetation (GV) means chlorophyllous vegetation.
3. Built-up area (BU) contains buildings, roads and every manmade imperious surface.
4. Bare land (BL) contains non-surface coverage such as soil and some incomplete built-up areas.

In this research, endmember extraction was performed in 2 steps: region selection and spectral library development. The regions are extracted from the image data through visual interpretation, and the spectral library is developed. Each region contains a set of spectra that are categorized based on endmember definitions. The number of regions (spectra) in each endmember is based on the complexity of ground features. After this step, six original spectral libraries are individually built.

Optimal spectra selection

Optimal spectra are chosen from the extracted endmember spectra using the endmember average RMSE (EAR), which was proposed by Dennison and Roberts in (2003). The equation can be expressed as follows:

$$EAR_{A_i,A} = \frac{\sum_{j=1}^n RMSE_{A_i,A_j}}{n - 1} \tag{4}$$

where A is the endmember class, A_i and A_j are the modeled spectra class, n is the number of spectra in class. The term $n - 1$ accounts for the endmember modeling, which produces a zero RMSE. EAR is calculated for each endmember spectrum as the average of the RMSE from a set of models, including the endmember spectrum, to unmix the other spectra in the same endmember land-cover class. Although EAR does not represent the purity of an endmember, it allows one to choose the appropriate endmember in the unmixing process. The spectrum in the class with lowest EAR was considered as the optimal endmember spectrum that best represented that class. The optimal endmember spectra in different time series are shown in Table 2.

Spectral unmixing

Two-endmember models were applied in this study because (1) a large number of endmember models may cause spectral confusion, (2) the number of model improvements may yield a lower RMSE but may not significantly change the endmember fraction and (3) more endmember models will result in a decreasing computational efficient. Photometric shade (SHD) was added as the endmember to account for the variation in illumination. According to previous studies (Dennison and Roberts 2003; Roberts et al. 1998; Townshend et al. 2000; Michishita et al. 2012a), the fractions of 1.05 maximum and -0.05 minimum are constrained. The additional range

Table 2 Number of optimal endmember spectra in different time series

Year	Endmember spectra number				
	Vegetation	Bare land	Built-up area	Water	Total
1991	8	2	5	3	18
1996	6	2	5	3	16
2000	5	1	5	2	13
2005	5	1	7	2	15
2009	6	1	7	3	17
2013	5	1	7	2	15

of 5 % was incorporated to take noise-oriented modeling errors into account (Rashed et al. 2003). The RMSE of each pixel is constrained to less than 0.025. A pixel was left unmodeled (Unm) when no model met the constraints.

Results and analysis

Accuracy assessment

Due to the lack of fractional reference data, the accuracy assessment could not be conducted in this research. However, the pixel level confusion matrix can be calculated. Thus, we combine the model into four ground feature categories and 500 pixels are selected randomly in each category and in each year. These pixels obey the same rules as the endmember extraction and are equally distributed in the corresponding image. The confusion matrices, the overall accuracy and the Kappa coefficient are shown in Table 3.

Although green vegetation and water areas are classified with high accuracy, bare land is classified with relatively low accuracy. In the research, bare land is defined as non-surface coverage such as soil and some incomplete built-up areas. There is some confusion in the built-up areas and bare land, which according to image interpretation is mostly distributed on the edges between urban and rural areas.

The Kappa coefficients of the six images are 0.76, 0.87, 0.73, 0.86, 0.74 and 0.68, which are not as high as some published classification algorithms but are still considered acceptable for the following reasons. First, the four ground feature categories were combined by the unmixed model. For example, eighteen models were generated for 1991 (Table 2). In other words, we actually classified eighteen categories. The Landsat spectral resolution is insufficient to support a very high accuracy in such classification categories. Second, a huge area was chosen in this research (nearly 811 km²). This area surely contained tremendous variations of land-cover types, potentially leading to confusion. Third, the result satisfies the demands of our research. The land cover's change tendency is clear from this accuracy.

Land-cover area change analysis

The land-use dynamics are determined to reveal the land-cover change, which can be expressed as

$$A_v = \frac{A_e - A_s}{A_s} \times \frac{1}{T} \times 100 \% \quad (5)$$

where A_v is the land-cover rate of change, A_e and A_s represent the same land-cover area in 2 image epochs. It

Table 3 Confusion matrix and accuracy coefficient of each year

Category 1991 ^a	Unm	BU	GV	W	BL	Total
Unmodel	0	0	0	0	63	63
BU	0	376	0	9	28	413
GV	0	97	500	0	113	710
W	0	13	0	491	20	524
BL	0	14	0	0	276	290
Total	0	500	500	500	500	2000
1996 ^b						
Unmodel	0	0	0	0	1	1
BU	0	440	4	0	117	567
GV	0	2	495	13	4	514
W	0	0	0	487	0	487
BL	0	58	1	0	378	437
Total	0	500	500	500	500	2000
2000 ^c						
Unmodel	0	0	0	0	10	10
BU	0	394	0	0	270	664
GV	0	1	481	2	1	485
W	0	20	0	498	0	518
BL	0	85	19	0	219	323
Total	0	500	500	500	500	2000
2005 ^d						
Unmodel	0	2	0	0	0	2
BU	0	495	35	8	128	666
GV	0	0	459	3	19	481
W	0	0	0	489	0	489
BL	0	3	6	0	353	362
Total	0	500	500	500	500	2000
2009 ^e						
Unmodel	0	0	0	0	0	0
BU	0	444	3	0	308	755
GV	0	1	496	0	18	515
W	0	0	0	500	0	500
BL	0	55	1	0	174	230
Total	0	500	500	500	500	2000
2013 ^f						
Unmodel	0	0	0	0	0	0
BU	0	444	3	0	308	755
GV	0	1	496	0	18	515
W	0	0	0	500	0	500
BL	0	55	1	0	174	230
Total	0	500	500	500	500	2000

^a Overall accuracy = (1643/2000) = 82.15 %; Kappa coefficient = 0.76

^b Overall accuracy = (1800/2000) = 90.00 %; Kappa coefficient = 0.87

^c Overall accuracy = (1592/2000) = 79.60 %; Kappa coefficient = 0.73

^d Overall accuracy = (1796/2000) = 89.80 %; Kappa coefficient = 0.86

^e Overall accuracy = (1614/2000) = 80.70 %; Kappa coefficient = 0.74

^f Overall accuracy = (1506/2000) = 75.30 %; Kappa coefficient = 0.68

Table 4 Area of different land covers of Wuhan from 1991 to 2013

Category	Area(Km ²)					
	1991	1996	2000	2005	2009	2013
BU	201.98	218.07	277.52	350.52	326.78	395.60
GV	463.73	377.03	314.58	302.89	326.99	225.72
W	234.94	181.74	220.12	205.95	185.71	177.95
BL	48.91	146.42	102.47	78.41	100.65	11.78

Table 5 Variation of land-use dynamic of Wuhan from 1991 to 2013

Category	Land-use dynamic					
	1991–1996	1996–2000	2000–2005	2005–2009	2009–2013	1991–2013
BU (%)	1.59	6.82	5.26	−1.69	5.20	4.36
GV (%)	−3.74	−4.14	−0.74	1.99	−7.74	−2.33
W (%)	−4.53	5.28	−1.29	−2.46	−1.04	−1.10
BL (%)	39.87	−7.50	−4.70	7.09	−22.07	−3.45

equals the fraction multiply by a pixel of the representative area of 900 square meters. T denotes the time interval. In addition, water bodies are not affected by fractional representation, so each water body pixel represents 900 square meters.

Tables 4 and 5 show the land use/cover change condition in Wuhan from 1991 to 2013:

1. Built-up areas show rapid growth from 1991 to 2013 at an average rate of 4.36 %. Vegetation, water body and bare land decreased at average rates of −2.33, −1.1 and −3.45 %, respectively, over the same period. From an area perspective, built-up areas nearly doubled and green vegetation were reduced to half from 1991 to 2013. Water areas decreased by 56.99 km², which is nearly one-quarter of its original area at the beginning of the period.
2. Built-up areas changed most rapidly from 1996 to 2000 at an average rate of 6.82 %. This rate slowed in the following years and even became negative in 2005 to 2009. From 2009 to 2013, the rate then resumed its positive trend. This high overall rate of change for built-up areas demonstrates the rapid urban development that has occurred in Wuhan over the last 20 years.
3. Vegetation areas decreased over the whole period, especially from 2009 to 2013. However, vegetation areas slightly increased from 2005 to 2009. Built-up and green vegetation areas experienced abnormal conditions from 2005 to 2009 where their tendencies are in the opposite direction from the rest of time series. In particular, the correlation between the rates

of change for built-up areas and green vegetation areas is significantly positive.

4. Water bodies showed a decreasing tendency over the 20 years under study. However, they increased slightly from 1996 to 2000. The most severe variation in water areas primarily occurred during the first 15 years (1991–2005). The rate of decrease then slowed to 7.76 km² from 2009 to 2013 inclusive.
5. The variation in bare land fluctuated. In each period, the amount of bare land changed significantly from increasing or decreasing, especially from 1991 to 1996 and from 2009 to 2013. Our definition of bare land includes soil and incomplete built-up areas. Therefore, the urbanization process might have influenced these results and led to confusion in the extent of variations in bare land.

The key result of land use/cover change in Wuhan is the transformation of the natural landscape to anthropogenic urban built-up areas. However, this transformation did not occur smoothly. The trend for water areas from 1996 to 2000 ran contrary to the rest of the period and from 2005 to 2009, the rate of growth in built-up areas became negative, whereas that for green vegetation areas turned positive, which were also both opposite to the general trend.

Built-up area change and transfer analysis

To analyze the growth in built-up areas, time-series land-cover fraction (LCF) maps are generated (Fig. 3). The built-up areas from the 2013 image are extracted and masked over the other fractional maps. In these maps, red

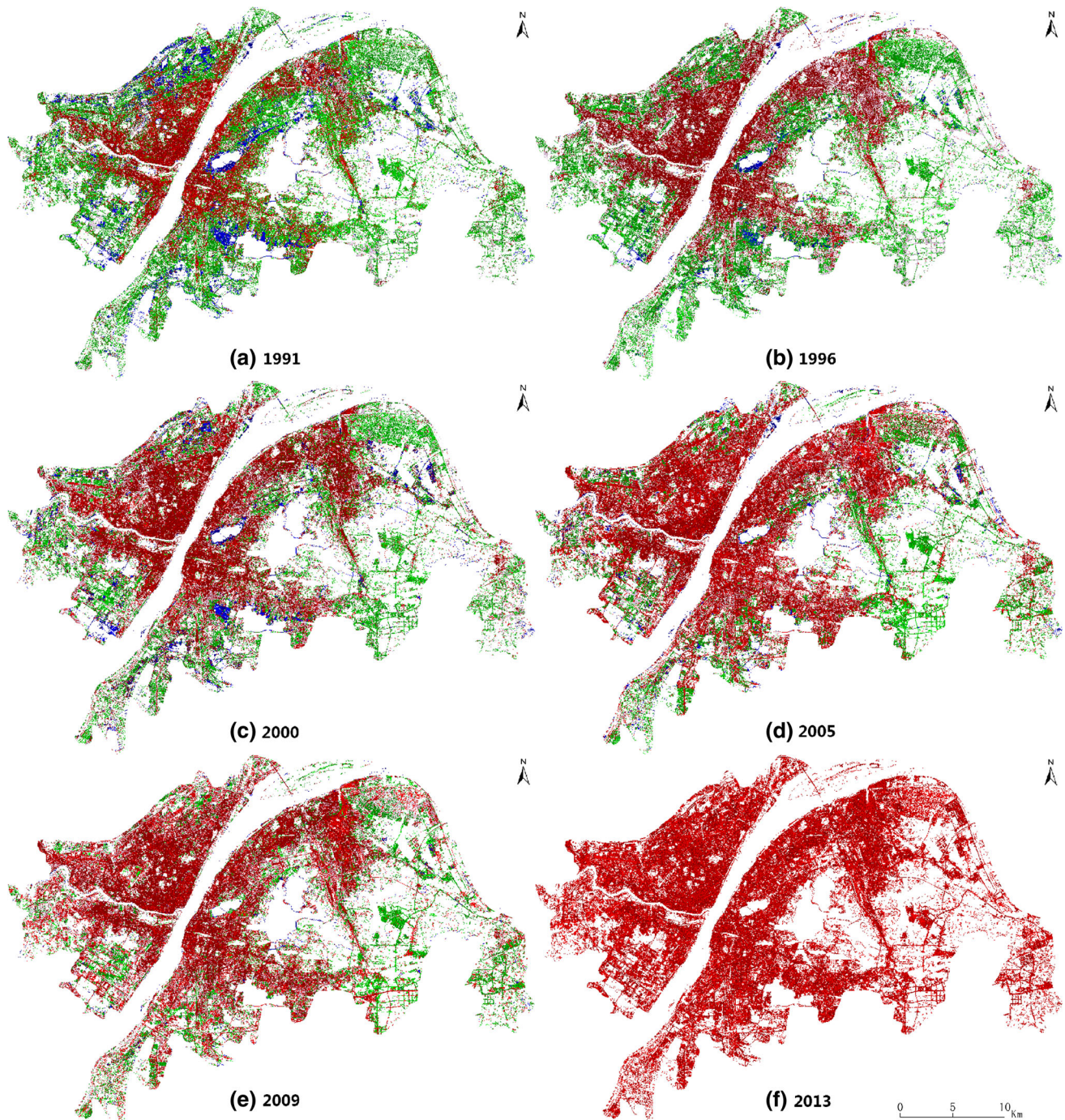


Fig. 3 Time-series land-cover fraction map: **a–f** for different years. *Red* is assigned to BU, *green* to GV, *blue* to water and *gray* to bare land, respectively. Pixels with high fraction have *brighter tones* and lower fraction have *darker tones*

is assigned to built-up areas, green to green vegetation areas, blue to water areas and gray to bare land areas, respectively. The green vegetation areas, water areas and bare land areas were finally transformed into built-up areas in 2013. Pixels with high fractions have brighter tones and lower fractions have darker tones.

The LCF maps reveal the following:

1. Spatially, the expansion of built-up areas extended outward from the geographic center of Wuhan, which is the intersection of the Han River and the Yangtze River. The three towns in Wuhan showed different

patterns of urban growth. The built-up area of Hankou was based in the old town and developed layer by layer in an arc. In Hanyang, the built-up area developed at a slow rate, primarily along the south of the Yangtze River and west of the Han River. The built-up areas in the old towns of Wuchang and Qingshan were slowly connected before 2000. Later, there was an expansion of economic development areas to the east of Wuhan.

2. Lake areas, which were encroached upon by built-up areas, primarily existed before 2005. Compared Fig. 3c with Fig. 3d, the blue area suddenly disappeared. This comparison reveals the deteriorating situation with respect to the lakes over only a five-year period. After then, these situations were prevented with effective government supervision. We also note that in the top left of Fig. 3c, some blue areas appeared. According to the government’s policy, some cultivated fields were forced to become fishery areas, which explains why the water areas showed an abnormal increase during this time series.

In particular, the red areas in these maps turned bright from Fig. 3a–f, which indicates that the fraction of built-up areas declined in these years, especially in the city center.

Urbanization process analysis

To understand the urbanization process in Wuhan, research by Michishita (2012b) is referenced to calculate the LCCI and to extract the dominant LCCI (DLCCI). LCCI was used to derive the average change in the area of each land-cover classification per day in each pixel between two observation dates of remotely sensed data. It is calculated using the following equation:

$$LCCI = \frac{LCF_{t1} - LCF_{t2}}{\Delta t} \times A \tag{6}$$

where LCF_{t1} and LCF_{t2} are two TM observation dates. Δt is the number of interval days between the two observation dates, and A is a pixel of the representative area, that is, 900 square meters.

Based on the concept of LCCI, two mechanisms of urban growth are defined: urban new land development and urban redevelopment. New land development means that another land-cover classification became built-up area that has high LCCI in both the built-up area and other land-cover types. Urban redevelopment refers to the reconstruction of a built-up area without a transfer of land-cover classification. Therefore, it has a high LCCI in the built-up area and a relatively low LCCI in other land-cover types.

The land-cover change intensity during each period is shown in Table 6, which reveals that in 1996–2000, vegetation and water bodies varied greatly, similar to built-up

Table 6 Variation of land-cover intensity

Time	Average LCCI (m ² /day)			
	Built-up area	Green vegetation	Water body	Bare land
1991–1996	0.03	−0.11	−0.15	0.29
1996–2000	0.12	−0.12	0.11	−0.20
2000–2005	0.10	−0.02	−0.04	−0.15
2005–2009	−0.04	0.04	−0.07	0.13
2009–2013	0.09	−0.25	−0.03	−0.53

areas. The same situation occurred from 1991 to 1996 and from 2009 to 2013. These three periods can be classified as urban development. From 1996 to 2000, green vegetation and water body areas varied relatively more slowly, but there was still a high LCCI for built-up areas. This period can be classified as urban redevelopment. From 2005 to 2009, built-up areas showed an abnormal, negative change. We believe that the existing built-up areas, especially on the urban fringe, were likely misclassified as bare land because of unbuilt construction.

DLCCI extraction for BU and GV can be expressed through the following equation:

Vegetation :

$$DLCCI_{GV,p} = (|Min(LCCI_{GV,P1}, LCCI_{GV,P2} \dots LCCI_{GV,Pn})|, P) \tag{7}$$

Built – up area :

$$DLCCI_{BU,p} = (|Max(LCCI_{BU,P1}, LCCI_{BU,P2} \dots LCCI_{BU,Pn})|, P) \tag{8}$$

P1, P2...Pn represent time series, and P is the point in time at which the absolute LCCI value reached its maximum. We export the maximum LCCI in built-up areas and the minimum LCCI in vegetation areas to determine the most extreme variation in the time series. Based on our images and the LCCI values, 5 time categories and 3 intensity categories are defined. The DLCCI provides a general illustration of the period during which the urbanization process reached its relatively high rate.

According to Fig. 4, from 1991 to 1996, vegetation areas decreased in a circular pattern around the old area of Wuhan (Circle 3). Comparing circle 1 and circle 3, built-up areas did not fill this gap immediately but instead developed slowly in a near-circular pattern in the following years. This development pattern gradually became negligible and finally stopped. Then, the inner-city areas began to experience redevelopment and reconstruction. The built-up area intensity did not change drastically, but expanded throughout a broad area outside the old town, including, for example, the Optics Valley area, the Wuhan Railway

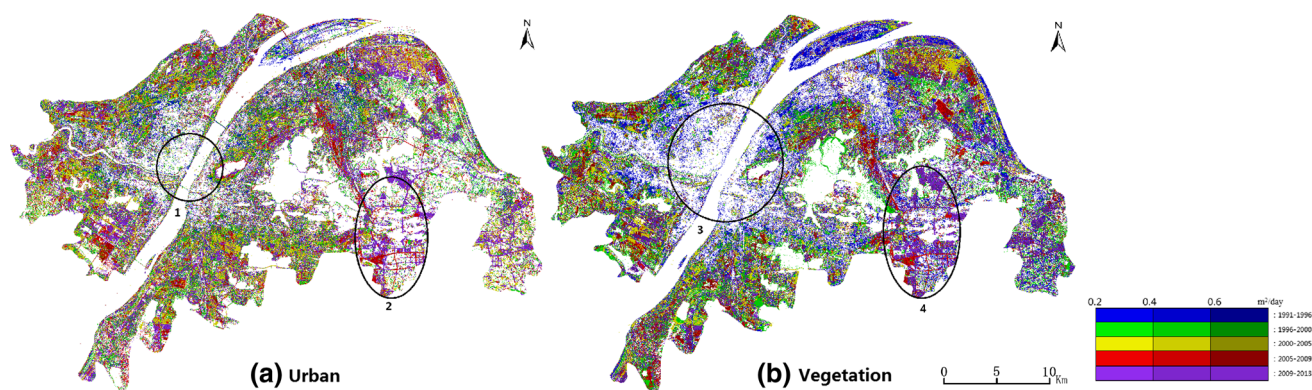


Fig. 4 DLCCI of urban and vegetation area

Station area and the Yanxi Lake area (Circle 2), all of which are referenced on the Wuhan electronic map. It is clear that the increase in built-up areas and decrease in vegetation areas were very consistent.

As shown above, Wuhan's urbanization process occurred in several steps from 1991 to 2013. It began at its geographic center with a circular pattern of expansion. Before 2000, the separate districts were gradually connected. In the next 4 years, reconstruction took over. Then, some built-up areas were developed rapidly outside of the old town. This urbanization process clearly changed Wuhan's natural landscape. Water areas, which decreased rapidly in the early years, have become carefully protected and were no longer destroyed after 2005. However, urbanization caused a substantial loss of agricultural land, especially in the later years.

Discussion

Endmember extraction

In previous studies, endmembers have been derived from an image or from an existing spectral library. In this study, the endmembers were primarily chosen through the visual interpretation of images. Some high-resolution Google Earth maps were also referenced. We characterized the different ground features in both TM images and Google Earth maps and chose the region of interest. Because Google Maps did not exist before 2000 and the TM images capture different data, it was impossible for us to ensure the purity of spectra of the whole region. In the following step, the appropriate endmembers are chosen and optimized. However, this process still influences the accuracy assessment, especially for some easily confused land objects. Some different image transformation approaches can be used to transform the multispectral images into a new image feature space. Next, the endmembers can be derived

from the extremes of this space by assuming that they represent the purest pixels in the images. For example, Lu and Weng (2006) uses the minimum noise-fraction procedure to select four endmembers: high-albedo, low-albedo, vegetation and soil. Nevertheless, the endmembers could not match the exact ground features and the procedure is not suitable to analyze complex land-cover changes in detail.

Another possible advantage is that endmembers' spectra are collected individually from six time images. It is very difficult to build a public spectral library for long-time-range data because of the different atmospheric situations, and the land surface in Wuhan rapidly changed over the twenty-year period. The strategy based on individually selecting ground materials leads to a more accurate assessment, especially in built-up areas. In addition, the combined endmember spectra ignore atmospheric effects between epoch images, which, as documented in previous research (Song et al. 2001), are extremely difficult to completely remove. However, we must combine the categories after spectral unmixing for further comparison and analysis using this collection method. Thus, a unified judgment cannot be established in the following step; it is necessary to optimize these methods in further research.

Unmixing result and accuracy assessment

A two-endmember model is used in this study to unmix the pixels in six temporal images. Based on some constraints, several units are categorized as unmodeled pixels. As shown in Table 7, the unmixing results are acceptable. The most successfully modeled image is from 2000, for which modeling achieved 99.83 %.

In addition, the 2013 image is referred to because its successful proportional modeling is lower than for the other five periods. We found that most of the unmodeled pixels are concentrated in the newly built industrial zone. Several experiments were attempted to extract more

Table 7 Number of land-cover models and the proportion of successfully unmixed pixels

Years	Endmember spectra number	Successfully proportion (%)
1991	18	99.54
1996	16	99.81
2000	13	99.83
2005	15	99.27
2009	17	99.69
2013	15	94.14

endmember spectra in these areas, but they ultimately failed because they could cause spectral confusion and thus decrease the accuracy of classification in other areas.

Because of the lack of reference data, an accuracy assessment could not be conducted in this research. Thus, a compromise method is chosen. Confusion matrices are calculated to conduct an accuracy assessment in the same manner as a hard classification method. The useful reference data should be available for a future study to conduct an accuracy assessment at the fractional level.

Conclusion

In this research, multiple endmember spectral mixture analysis (MESMA) was used to solve the mixed-pixel problem in Wuhan's urban area. Six endmember spectra libraries were built individually, and a two-endmember model was used to unmix the pixels. Then, the land use/cover change and urbanization process in the Wuhan area from 1991 to 2013 were analyzed. Our conclusions are as follows:

1. By extracting the endmembers and unmixing the pixels in the images with two-endmember models, the land-cover type and fractional information are successfully acquired. Then, we combine these data to generate a time-series LCF map and a DLCCI map to analyze Wuhan's urbanization pattern in a visualized way.
2. The Wuhan urban area experienced extensive development from 1991 to 2013. Built-up areas showed rapid growth from 1991 to 2013 at a rate of 4.36 %, with the fastest rate occurring from 1996 to 2000, at 6.82 %. Then, the speed of development slowed and became negative from 2005 to 2009. However, it became positive again from 2009 to 2013. The rate increased at the expense of a decrease in vegetation areas and inner-city lakes. However, the green vegetation and water areas did not decrease smoothly. The trend of variation in water areas from 1996 to 2000 ran contrary to that of the rest of the period, whereas from

2005 to 2009, the trend for green vegetation areas turned positive.

3. The urbanization process is strongly related to time and space. Before 2000, the urban growth pattern emphasized new land development, centralized and extending out from the geographic center of Wuhan. Urban growth developed at a relatively slow rate in a nearly circular pattern. The three towns of Wuhan showed different rates of spatial urbanization. From 2000 to 2005, the inner city focused more on urban redevelopment. On this basis, the built-up areas expanded outside of the old town, especially from 2009 to 2013. The increasing intensity during this period was nearly the same as in the early years, but the size of the area was much more extensive. This pattern is highly consistent with that decrease in vegetation areas.

Acknowledgments This work was funded in part by the National Natural Science Foundation of China (61601418), in part by the CRSRI Open Research Program (CKWV2013221/KY), in part by the Natural Science Foundation of Hubei Province (2012FFB06501), and in part by the National High Technology Research and Development Program of China (2012AA121303).

References

- Adams JB, Smith MO, Gillespie AR (1993) Imaging spectroscopy: Interpretation based on spectral mixture analysis. In: Pieters CM and Englert P (eds) Cambridge University Press, New York, pp 145–166
- Alan HS, Curtis EW, James AS (1986) On the nature of models in remote sensing. *Remote Sens Environ* 20(2):121–139
- Chen BM (1997) Studies on land use and land cover change in china and man's driving force upon it. *Nat Resour* 2:31–35 (**In Chinese**)
- Chen T, Niu RQ, Li PX, Zhang LP, Du B (2011a) Regional soil erosion risk mapping using RUSLE, GIS, and remote sensing: a case study in Miyun Watershed. *North China Environ Earth Sci* 63(3):533–541
- Chen T, Niu RQ, Wang Y, Li PX, Zhang LP, Du B (2011b) Assessment of spatial distribution of soil loss over the upper basin of Miyun reservoir in China based on RS and GIS techniques. *Environ Monit Assess* 179(1–4):605–617
- Cracknell AP (1998) Synergy in remote sensing—what's in a pixel? *Int J Remote Sens* 19:2025–2047
- Dennison PE, Roberts DA (2003) Endmember Selection for multiple endmember spectral mixture analysis using endmember average RMSE. *Remote Sens Environ* 87:123–135
- Fisher P (1997) The pixel: a snare and a delusion. *Int J Remote Sens* 18:679–685
- Huang W, Zeng Y, Li S (2015) An analysis of urban expansion and its associated thermal characteristics using landsat imagery. *Geocarto Int* 30:93–103
- Lu DS, Weng QH (2006) Use of impervious surface in urban land-use classification. *Remote Sens Environ* 102(1–2):146–160
- Michishita R, Gong P, Xu B (2012a) Spectral mixture analysis for bi-sensor wetland mapping using Landsat TM and Terra MODIS data. *Int J Remote Sens* 33(11):3373–3401

- Michishita R, Jiang Z, Xu B (2012b) Monitoring two decades of urbanization in the Poyang Lake area, China through spectral unmixing. *Remote Sens Environ* 117:3–18
- Montgomery MR (2008) The urban transformation of the developing world. *Science* 319:761–764
- Niu RQ, Du B, Wang Y, Zhang LP, Chen T (2014) Impact of fractional vegetation cover change on soil erosion in Miyun reservoir basin. *China Environ Earth Sci* 72(8):2741–2749
- Powell RL, Roberts DA (2010) Characterizing urban land-cover change in Rondônia, Brazil: 1985 to 2000. *J Lat Am Geogr* 9(3):183–211
- Powell RL, Roberts DA, Dennison PE, Hess LL (2007) Sub-pixel mapping of urban land cover using multiple endmember spectral mixture analysis: manaus, Brazil. *Remote Sens Environ* 106:253–267
- Rashed T, Weeks JR, Roberts D, Rogan J, Powell R (2003) Measuring the physical composition of urban morphology using multiple endmember spectral mixture models. *Photogramm Eng Rem S* 69:1011–1020
- Ridd MK (1995) Exploring a V-I-S (vegetation-impervious surface-soil) model for urban ecosystem analysis through remote sensing: comparative anatomy for cities. *Int J Remote Sens* 16:2165–2185
- Roberts DA, Gardner M, Church R, Ustin S, Scheer G, Green RO (1998) Mapping chaparral in the Santa Monica Mountains using multiple endmember spectral mixture models. *Remote Sens Environ* 65(3):267–279
- Roberts DA, Dennison PE, Ustin SL et al (1999) Development of a regionally specific library for the Santa Monica Mountains using high resolution AVIRIS data. In: Proceedings of the eight AVIRIS earth science workshop. Jet Propulsion Laboratory, Pasadena, pp 349–354
- Rosso PH, Ustin SL, Hasting A (2005) Mapping marshland vegetation of SanFrancisco Bay, California, using hyperspectral data. *Int J Remote Sens* 26(23):5169–5191
- Small C (2001) Estimation of urban vegetation abundance by spectral mixture analysis. *Int J Remote Sens* 22(7):1305–1334
- Small C (2002) Multitemporal analysis of urban reflectance. *Remote Sens Environ* 81:427–442
- Song C, Woodcock CE, Seto KC, Lenney MP, Macomber SA (2001) Classification and change detection using Landsat TM data: when and how to correct atmospheric effects? *Remote Sens Environ* 75(2):230–244
- Townshend JRG, Huang C, Kalluri SNV, Defries RS, Liang S, Yang K (2000) Beware of per-pixel characterization of land cover. *Int J Remote Sens* 21(4):839–843
- United Nations, Department of Economic and Social Affairs, Population Division (2012) World urbanization prospects: the 2011 revision
- Weng Q, Quattrochi D (2007) An introduction to urban remote sensing. In: Weng Q, Quattrochi D (eds) Urban remote sensing. CRC Press, Florida
- Wuhan Municipal Bureau of Statistics (2012) National economic and social development statistical bulletin in 2012 of Wuhan city
- Zhao et al (2003) Remote sensing application principle and method. Science Press, Beijing (**In Chinese**)